

CLASSY VII: Ultraviolet Radiation Transfer Modeling of Outflows in Local Star-Forming Galaxies

MASON HUBERTY,¹ CODY CARR,¹ CLAUDIA SCARLATA,¹ XINFENG XU,² TIM HECKMAN,² DANIELLE BERG,³
STÉPHANE CHARLOT,⁴ JOHN CHISHOLM,³ ALAINA HENRY,^{2,5} BETHAN JAMES,⁶ CRYSTAL MARTIN,⁷ AND MATILDE MINGOZZI⁵

¹*Minnesota Institute for Astrophysics, University of Minnesota, Minneapolis, MN 55455, USA*

²*Center for Astrophysical Sciences, Department of Physics Astronomy, Johns Hopkins University, Baltimore, MD 21218, USA*

³*Department of Astronomy, The University of Texas at Austin, 2515 Speedway, Stop C1400, Austin, TX 78712, USA*

⁴*Sorbonne Université, CNRS, UMR7095, Institut d'Astrophysique de Paris, F-75014, Paris, France*

⁵*Space Telescope Science Institute, 3700 San Martin Drive, Baltimore, MD 21218, USA*

⁶*AURA for ESA, Space Telescope Science Institute, 3700 San Martin Drive, Baltimore, MD 21218, USA*

⁷*Department of Physics, University of California, Santa Barbara, Santa Barbara, CA 93106, USA*

ABSTRACT

Massive outflows are an important component of a galaxy's evolution, regulating star formation and affecting the dynamics of the surrounding media. Extracting outflow information from absorption spectra is difficult, but radiation transfer modeling offers an insight into these processes. The emission and absorption features in spectra probe outflows, but are complex depending on many different parameters. Radiation transfer modeling has the potential to disentangle the underlying physics of the lines. As such, we analyze the signatures of galactic outflows in the spectra of local ultraviolet star-forming galaxies in the CLASSY survey using a semi-analytical line transfer method. These efforts are concentrated on the resonant lines of several ionization states of silicon that trace cool and warm gas, in order to study the geometric and physical characteristics of these gasses within the outflows. From the model constraints, we estimate the mass outflow rates for these galaxies and look for trends with other galactic properties. We compare our estimated relationships with those in previously established literature, and speculate reasons for similarities and deviations between this work and others. In addition, we derive momentum and energy outflow rates. We find that our semi-analytical method captures the same trends as Gaussian fitting techniques with regards to outflow rates; however the magnitude of these values often differs. Our work also reiterates the positive correlation between the mass outflows rate and star-formation rates. These results also suggest that the analyzed star-forming galaxies host momentum driven, as opposed to energy driven outflows.

1. INTRODUCTION

The mass ejection of gas into the circumgalactic medium via galactic outflows is omnipresent in star-forming galaxies (e.g. Shapley et al. 2003, Martin 2005). This phenomenon heavily regulates star-formation in galaxies, and thus is a large influence in the study of galactic evolution (Hopkins et al. 2014). One of the defining characteristics of outflows is the mass outflow rate, and numerous techniques have been used in the past to attempt to estimate this physical parameter for a diverse background of galaxies (e.g. Heckman et al. 2015, Chisholm et al. 2017, Xu et al. 2022). Mass outflow rates vary substantially across different galaxies and models, not only because outflow geometry can vary from biconical to spherical (e.g. Carr et al. 2021), but because the mass outflow rate technically varies with radius inside the outflow (Chisholm et al. 2017). That

said, determining the relationships between the mass outflow rate and other properties of a galaxy is useful in understanding how outflows behave in different environments.

The absorption and emission features originating from the outflowing gas observed in the spectra of outflows depend on numerous parameters such as the gas optical depth, outflow geometry, and dust opacity. This complexity demands high-spectral resolution observations to distinguish the spectral details and provide tighter constraints on the underlying physics governing the radiation transfer (Carr et al. 2022). A data set that provides such opportunity to model these galactic properties with radiation transfer theory is the COS Legacy Archive Spectroscopy SurveY (CLASSY as presented in Berg et al. 2022).

In Xu et al. (2022), Gaussian profiles were used to model the absorption and emission lines of the outflows

Table 1: Atomic Data for Si II Si III and Si IV ions. Data taken from the NIST Atomic Spectra Database^a

Ion	Wavelength (Å)	Type	$A_{ul}(s^{-1})$	f_{ul}
Si II	1190.42	Resonant	6.53×10^8	0.277
Si II	1193.28	Resonant	2.69×10^9	0.575
Si II	1194.50	Fluorescent	3.45×10^9	0.737
Si II	1197.39	Fluorescent	1.40×10^9	0.150
Si II	1260.42	Resonant	2.57×10^9	1.22
Si II	1265.02	Fluorescent	4.73×10^8	0.113
Si III	1206.50	Resonant	2.55×10^9	1.67
Si IV	1393.76	Resonant	8.80×10^8	0.513
Si IV	1402.77	Resonant	8.63×10^8	0.255

^a <http://www.nist.gov/pml/data/asd.cfm>

identified in the spectra of CLASSY galaxies. These models estimate the CLASSY outflow velocities, gas column densities, and the mass outflow rates for each galaxy. However, there are some limitations of this approach: absorption and emission features are modeled independently of each other, there is no way to account for a non-spherical outflow, and limits the number of parameters that could be extrapolated in contrast to an semi-analytical technique. On the other hand, radiation transfer modeling has the potential to provide tighter constraints on a wider range of parameters.

In this paper, we perform semi-analytical radiation transfer modeling of the emission and absorption features in the CLASSY galaxies as an alternative to Gaussian fitting procedures. We target the ultraviolet silicon resonant lines that trace cool and warm gas within outflows, and the resulting galactic properties and mass outflow rates that follow from the modeling of these lines.

This paper is structured as follows: In section 2, we discuss the CLASSY data and its importance. In section 3, we review the SALT model. In section 4, we discuss the fitting procedure and parameter estimates of SALT. The results of this analysis are discussed in section 5. A discussion of the mass outflow rates and their consequences follows in section 6. Comparisons to previous literature are included in section 7. Our conclusions are outlined in section 8.

This paper assumes standard cosmology ($H_0 = 70 \text{ km s}^{-1} \text{ Mpc}^{-1}$, $\Omega_m = 0.3$, and $\Omega_\Lambda = 0.7$).

2. CLASSY

The COS Legacy Archive Spectroscopy SurVeY (CLASSY) provides high-resolution far-ultraviolet (FUV) Hubble Space Telescope observations of 45 nearby galaxies (Berg et al. 2022). This sample completes the FUV wavelength range in the observed frame between roughly 1200Å and 2000Å. This range includes

the silicon resonant absorption lines of Si II (1190.42Å, 1193.28Å, and 1260.42Å), Si III (1206.50Å), and Si IV (1393.76Å and 1402.77Å). It is these lines of silicon that we will use to analyze the properties of the galactic outflows in their host galaxies. Silicon II and III are good tracers of gas at around $T = 10^4 \text{ K}$, whereas silicon IV is a tracer of warmer gas of about 10^5 K (see Tumlinson et al. 2017). Si II is of particular interest, as this line is believed to trace neutral hydrogen gas (e.g. Shapley et al. 2003).

Observations within CLASSY were taken with the Cosmic Origins Spectrograph (COS) on the Hubble Space Telescope. In order to determine the star-forming region of each galaxy, R_{SF} , we use the NUV half-light radii (R_{50}) as defined and calculated in Xu et al. 2022 (The radius of the galaxy within which half the photons in the COS image are contained). However, for some of the CLASSY galaxies, the photon counts do not flatten at large radii, as a result of being close to or larger than the size of the COS aperture. In these cases ($r_{50} > 0.35''$), SDSS u-band sizes are adopted instead (as in Xu et al. 2022).

As discussed in Carr et al. (2021), due to the aperture size of an observing instrument, SALT needs to account for spectral information that lies beyond a projected radius, R_{AP} , for which the corresponding velocity field is v_{AP} . COS has an aperture diameter of $2.5''$, and therefore we would take the radius of the aperture of the observing instrument, R_{AP} , to be the projected COS aperture radius on each galaxy, i.e. the physical distance of $1.25''$ at the red-shift of that galaxy in kPc . However, we modify this size for this study: The COS throughput in the NUV drops below 80% roughly at the offset of 0.7 arcseconds from the center, which we take to be R_{AP} for this study. It turns out this adjustment fits the data better (further commented on in Section 4).

In order to determine if the spectra of the 45 galaxies were viable for analysis, we first visually inspected the wavelength ranges of interest. In some cases, there was no coverage in the region of interest; in this case, the line is not modeled (although other lines from that same galaxy may still be modeled). The spectrum is also not modeled if there is too much noise in the region of interest. For example, the proximity of the Si III line to the geocoronal $Ly\alpha$ line of the milky way, occasionally results in no observable P-Cygni profile at 1206.50Å. As a result, seven galaxies are not modeled at the Si II 1190.42/1193.28Å wavelength range, thirteen galaxies at the Si II 1260.42Å wavelength range, and fifteen galaxies at the Si III 1206.50Å wavelength range were not analyzed.

In the event that a part of the wavelength range has to be thrown out due lack of data or noise (such as a galaxy's 1260.42\AA being unusable, but the $1190.42/1193.28\text{\AA}$ is usable or the 1393.76\AA line is usable but the 1402.77\AA line is not), only the usable portion of the spectrum is fit with SALT. Galaxies with only partial fits are indicated in the Table ? and sample plots in the Appendix.

We normalize the spectra to the stellar continuum (see Xu et al. 2022). If the presence of the Milky Way's Lyman α line resulted in a poor normalization of the absorption lines of interest, we manually renormalized the spectra to the surrounding continuum.

3. SALT MODELING

The Semi-Analytical Line Transfer (SALT) Model, as outlined in Scarlata & Panagia (2015), provides a case for the modeling of absorption and emission lines of spherical galactic outflows. This technique of developing a model for the observed spectra of galaxies has been used and adapted in Carr et al. (2018) and again in Carr et al. (2022), and has been used in the study of the properties of outflows in green pea galaxies (low mass, low metallicity, high star formation galaxies - see Carr et al. (2021)).

The SALT model pictures a spherical galaxy with an associated outflow that behaves as a series of concentric, expanding shells (Scarlata and Panagia (2015)). Photons from the galaxy are emitted uniformly in all directions, which then pass through the outflow, leading to elementally associated absorption and emission of said photons. The advantage of using the SALT model for analyzing P-Cygni profiles is that it consistently computes the absorption and re-emission, thus automatically accounting for emission inflowing. Carr et al. (2018) included the modification of the geometry of the outflow to allow for biconically-shaped outflows.

SALT models the outflows with the following parameters; assuming that the velocity and density fields are power-laws (as in Carr et al. 2018, 2021):

- α , the opening angle of the bicone.
- ψ , the orientation angle of the bicone.
- γ , the wind velocity gradient of the gas.
- δ , the density gradient of the gas.
- τ_0 , the optical depth of the gas.
- f_c , the covering fraction of the outflow gas.
- k , the dust opacity.

- v_0 , the launch velocity of the gas in the outflow (the velocity at R_{SF}).
- v_w , the terminal velocity of the gas in the outflow (the velocity at R_w).
- v_{AP} , the velocity at the maximum radius observed withing the aperture of the observing instrument.

As in Carr et al. (2021), we constrain the aperture velocity:

$$v_{AP} = v_0 \left(\frac{R_{AP}}{R_{50}} \right)^\gamma. \quad (1)$$

We also constrain the dust opacity, k , using the measured color excess and assuming a Calzetti extinction law to compute A_{UV} . We convert A_{UV} to the dust optical depth with $A_{UV} \approx 1.086\tau_{UV}$. The dust optical depth and the dust opacity in the code are related by

$$\tau_d = \begin{cases} \frac{k}{\gamma} \ln\left(\frac{v_w}{v_0}\right) & \text{if } \delta = 1 \\ \frac{k}{1-\delta} \left[\left(\frac{v_w}{v_0}\right)^{(1-\delta)/\gamma} - 1 \right] & \text{otherwise.} \end{cases} \quad (2)$$

We extend SALT modeling to also include an absorption component at systematic velocity, which we use to describe absorption in the interstellar medium (ISM) of the galaxy. The presence of an interstellar medium component requires the addition of two additional parameters. We assume that any ISM absorption or emission component takes the form of a Gaussian (Xu et al. 2022, Carr et al. 2022 etc.).

- a , the height/depth of the Gaussian profile.
- σ , the width of the profile.

The ISM component is accounted for in the intrinsic profile, prior to any radiation transfer modeling with SALT. Thus in total, 8 free parameters are required to be fit with SALT; with the possible of 2 more free parameters for lines hosting a significant ISM component (a and σ).

In this study, we also considered models of a spherical SALT model (in which $\alpha = 90^\circ$, ϕ is irrelevant), with a modification of the wind covering fraction that allows for a power law over radius: $f_c = a_1 y^{-b_1}$. However, spherical SALT fits with this covering fraction resulted in b_1 values at a very small scale (ranging from 10^{-2} to 10^0). This small value close to 0 led us to the conclusion that f_c tends to be constant with radius, and thus as the spherical model is within the bicone model space, the bicone model is generally a more advantageous model, to allow for different geometry of outflows, in addition to the purely spherical one. The biconical model does contain two additional parameter relative to

Table 2: Milky Way Lines Considered While Masking

Ion	Wavelength (Å)
H I	1215.67
C I	1277.21
C II	1334.53, 1335.71
N I	1199.55, 1200.22, 1200.71
N V	1235.81, 1242.80
O I	1302.17
Si II	1190.42, 1193.28, 1260.42, 1304.37
Si III	1206.50
Si IV	1393.76, 1402.77
S II	1250.59, 1253.81, 1259.52

the spherical one, but repeated AIC and BIC comparisons between the spherical and biconical models fitted to CLASSY lines showed little evidence to suggest that the spherical model was more favorable to the biconical one in the vast majority of tests.

The relevant resonant and fluorescent absorption and emission wavelengths that are analyzed are included in Table 1. The Si II 1190.42, 1193.28, and 1260.42Å lines are all modeled together (where possible), where all SALT parameters are kept consistent across all three absorption lines, with the exception of the ISM parameters (a and σ , because we do not perform any radiation transfer modeling in the ISM. Likewise, for the Si IV 1393.76Å and 1402.77Å lines, SALT models these two lines together (as was done in Carr et al. 2021), again with all the parameters kept the same except for the ISM parameters.

SALT assumes that the aperture of the observing instrument, in this case the COS onboard the Hubble Space Telescope, is larger than the star-forming region of the target galaxy. Therefore, any galaxies with a COS radius larger than R_{50} is not necessarily properly fitted with SALT. We still present the SALT fits of the lines in these galaxies, but we omit them from the subsequent analysis of mass outflow rates, when applicable (see Section 6). These galaxies are J0144+0453, J0337-0502, J0405-3648, J0934+5514, J0940+2935, J0944-0038, J1016+3754, J1105+4444, J1119+5130, J1132+5722, J1148+2546, J1150+1501, J1157+3220, J1225+6109, and J1444+4237.

We also mask Milky Way absorption lines that contaminate the spectra of our CLASSY galaxies. These lines appear in the rest frame of the Milky Way, and thus have no red-shift from their resonant lines. Relevant masking regions are included in table 2.

Masking is used during the fitting process, but any wavelength ranges with sufficiently overlapping outflow features and masks are also excluded from the fitting

Table 3: Free Parameter Fitting Ranges

Parameter	Range
v_0 (km s ⁻¹)	[2.0,150.0]
v_w (km s ⁻¹)	[200.0,1300.0]
γ	[0.5,2.0]
τ_0	[0.01,100.0]
f_c	[0.0,1.0]
α (°)	[0.0,90.0]
ψ (°)	[0.0,90.0]
a	[0.0,1.0]
σ (km s ⁻¹)	[0.0,500.0]

process, as it becomes too difficult to distinguish the two. As a result of masking, an additional 22 Si II 1190.42/1193.28Å, 2 Si II 1260.42Å, and 3 Si IV 1393.76/1402.77Å wavelength ranges were not fit with SALT.

Upon inspection of the spectra in galaxy J1416+1223, the absorption lines for the relevant Si II, III, and IV ions were noted to be asymmetric and containing a significant red-shifted component, more indicative of a galactic inflow than an outflow (Rubin 2017, Carr et al. 2022). Therefore, we do not fit SALT to this galaxy. Three galaxies that were not fit for any absorption line of silicon are J0808+3948, J1044+0353, and J1323-0132; (the explanation for this is included alongside their spectra in the Appendix).

For the galaxies that had SALT fits in all three ionization states of silicon, the galaxies' size distributions can be seen in Figure 2. It is these galaxies that we will conduct the full mass outflow rate calculation in Section 6. The five galaxies above this line are J0405-3648, J0934+5514, J0940+2935, J1105+4444, and J1150+1501 (the HST/COS and SDSS r-band images of these galaxies can be found in Berg et al. 2022). Unfortunately, the consequence of this omission means a large population of the lower mass galaxies are omitted from our mass outflow analysis, as many of these large galaxies were at low-redshift and thus by selection were low mass galaxies.

4. SALT PARAMETER ESTIMATES

Through the use of the `emcee` Markov Chain Monte-Carlo sampler, the SALT code fits the outflow parameters to the masked normalized spectrum of the galaxy (Foreman-Mackey et al. 2013) using a maximum likelihood estimation (Ivezić et al. 2014).

The ranges allowed for the free parameters in the fitting process can be found in Table 3.

Parameter δ is a special case: The mass outflow rate should not deviate substantially from the constant mass

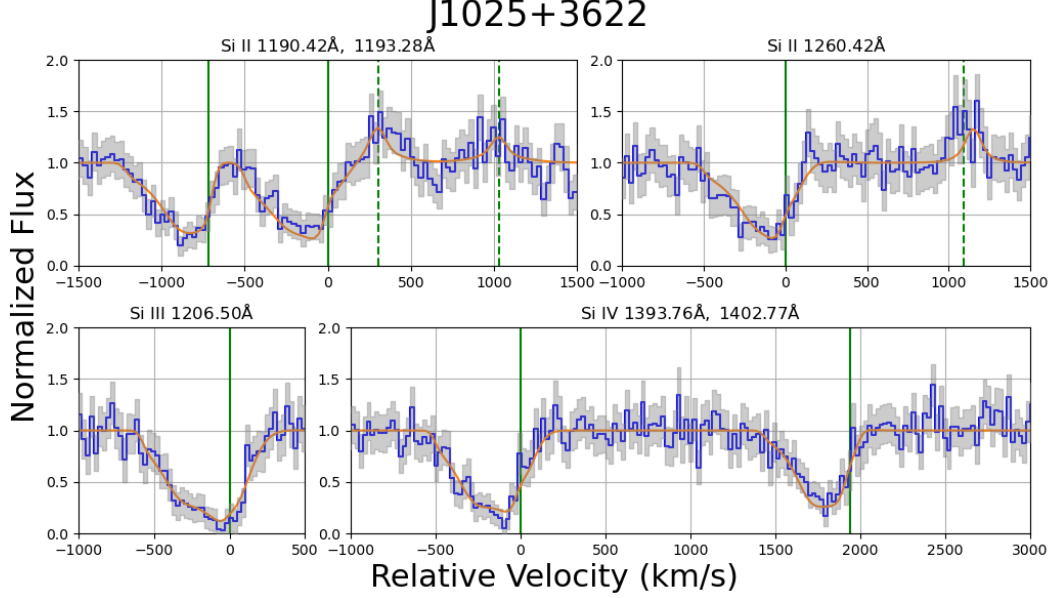


Figure 1: Example SALT fits for CLASSY galaxy J1025+3622.

outflow rate that would predict a value of $\delta = \gamma + 2$ (Carr et al. 2018). Therefore δ is restricted to be within a value of 1.5 from the constant mass outflow rate prediction, i.e. $\gamma + 0.5 \leq \delta \leq \gamma + 3.5$. The τ_0 parameter is sampled logarithmically, so that both small and large scale predictions for this parameter is tested.

During the `emcee` fitting process, after each model is generated, it undergoes a Gaussian smoothing, prior to being tested against the data. As many of the CLASSY galaxies are comparatively large relative to R_{COS} , we adjust the standard deviation of the Gaussian used in the smoothing for each galaxy. The deviation of this Gaussian is chosen as the physical size of the galaxy is determined from the COS arcseconds/Pixel ratio (0.0285) and the grating used to image the CLASSY galaxies (which has a ratio of 9.97mÅ/Pixel for the G130M images and 12.23mÅ/Pixel for the G160M images), which is then divided by the velocity separation of data points in each galactic spectrum. For galaxies with an R_{50} larger than R_{COS} , the angular size of the imaged galaxy is replaced with the angular size of COS (in which $R_{COS} = 0.7$ arcseconds). For these extended galaxies, if a value of 1.25 arcseconds is used instead, the resolution is too large and results in oversmoothing of the model, which creates a poor model fit to the data.

Uncertainties for each parameter are taken to be the median of the deviations of the parameter about the chosen maximum likelihood estimation parameter, from the MCMC chains. Once the fitting is complete, the fit is visually inspected. If the fit deviates from the CLASSY data to an extent that it appears the shape of the data

does not match that of the fit, the fitting process was repeated.

5. RESULTS

Example fits for each of the silicon lines for one of the CLASSY galaxies can be seen in **Figure 1**. The fits for all galaxies in CLASSY can be found in the **Appendix**. The best-fit parameters of the outflows derived modeling the Si II, III, and IV lines for each galaxy can be found in **Table 4**. In addition to the free and constrained parameters, the number density n_0 , the terminal radius R_w , and the column density N of the silicon ionization states was also computed. The relevant calculations are below:

$$n_0 = \frac{m\epsilon\tau_0v_0}{\pi e^2 R_{SF}}. \quad (3)$$

$$R_w = R_{SF} \left(\frac{v_w}{v_0} \right)^{1/\gamma}. \quad (4)$$

$$N = \begin{cases} n_0 R_{SF} \ln(R_w/R_{SF}) & \text{if } \delta = 1 \\ n_0 \frac{R_{SF} - R_w(R_w/R_{SF})^{-\delta}}{\delta - 1.0} & \text{otherwise.} \end{cases} \quad (5)$$

5.1. Geometry

Note abundance of spheres, large opening angles Do Si II, III, IV tend to overlap to some extent, but are often independent of each other. See **Table 4** and **Figure 11**.

5.2. ISM Model Selection

Galaxies can roughly be divided into three categories: (1): Those without a prominent ISM component, (2): Those with a prominent ISM absorption component,

and (3): Those with a prominent ISM absorption and a prominent ISM emission component. All lines were fit with all three of these models; the model that best fits the data is chosen as the most appropriate model for that absorption line for that galaxy. The advantage of these three models is that it removes any extra parameters that may be incorporated in the model. For example, if there is no major ISM component, it is inconvenient to add two extra parameters representing the ISM absorption (in fact, if these parameters are included in the modeling of an absorption line with no ISM, `emcee` still tries to add a Gaussian distribution, which actually makes the fit worse). In some cases, we see significant red and blue-shifted absorption around the absorption line, which could be due to turbulent broadening, which at present SALT has no capacity to compute. In this case an ISM absorption component with no ISM emission is the best way to proceed (it is evident in the spectra if no ISM emission is present in these situations).

Note the ISM emission/free vaperture redundancy here.

(NEED TO ADD A COMPARISON BETWEEN THE TWO? - WAIT ON THIS).

6. DISCUSSION

We now investigate the derived mass outflow rate of each galaxy, and the related momentum and energy outflow rates. In addition to finding relationships between these fluxes and other galactic properties, we also make predictions on the fundamental physics of these outflows, such as if they are momentum or energy driven processes.

6.1. Mass Outflow Rates

The derived outflow parameters can be used to calculate the mass outflow rate of the corresponding ions of silicon. The mass outflow rate (\dot{M}) is defined as the mass passing through a radius r within the outflow. We use

$$\dot{M}(r) = \Omega f_c m_{Si} n_{0,Si} v_0 R_{SF}^2 \left(\frac{r}{R_{SF}}\right)^{(2+\gamma-\delta)}. \quad (6)$$

where

$$\Omega = 4\pi(1 - \cos(\alpha)). \quad (7)$$

as the definition for the mass outflow rate, where m_{Si} is the mass of the silicon ion. Evidently, the mass outflow rate is dependent on the radius r , corresponding to a specific velocity v within the outflow (Burchett et al. 2021). We choose to present the mass outflow rates as calculated at $r = R_{SF}$, corresponding to $v = v_0$. This is done not only to establish a baseline comparison value between each CLASSY galaxy, but also to

CLASSY Galaxies' COS Radius vs. NUV 1/2 (R_{50}) Radius

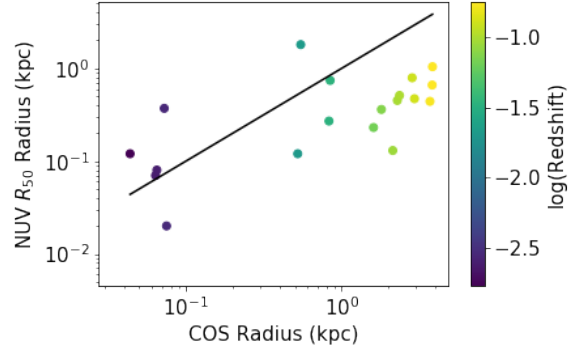


Figure 2: Size comparison between half-light radius (R_{50}) and the radius of the galaxy observed with the COS aperture. Galaxies above the black, one-to-one line are omitted from the SALT analysis, as SALT requires the star-forming region to be within the aperture of the observing instrument.

remove the dependence of this calculation on the γ and δ SALT parameters. The simulations conducted in Carr et al. (2022), suggests that these two free parameters in particular do not converge as well as the other SALT parameters.

In order to compute the total mass outflow rate for each galaxy, we must first determine the mass outflow rate for each of the individual ionization states of silicon. We assume that silicon only exists in the three ionization states of Si II, III, and IV (see Chisholm et al. 2018, Mckinney 2019 et al.); thus the total silicon mass outflow rate can be determined by summing the three individual components.

One consequence of this is that only galaxies that have successfully been fitted for the Si II, III, and IV lines can be included (i.e. fits must be obtained from all three states).

Given the metallicity of each CLASSY galaxy (referenced from Berg et al. 2022) relative to the solar metallicity and the ratio of hydrogen to silicon in the sun, we scale the silicon mass outflow rate to that of the hydrogen mass outflow rate:

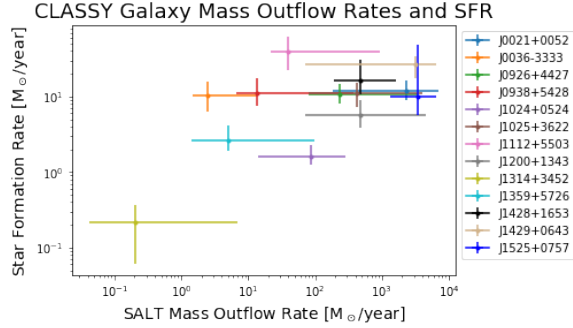
$$\dot{M}_H = \dot{M}_{Si} \frac{Z_{Galaxy}}{Z_{\odot}} \frac{n_{H,\odot}}{n_{Si,\odot}}. \quad (8)$$

The mass outflow rates for each relevant galaxy can be found in Table 3.

An important relation worth mentioning is the relationship between \dot{M} and the SFR, as seen in Figure 4. We note a direct correlation between \dot{M} and SFR, a relation found in other surveys of low-redshift galaxies (e.g. Heckman et al. 2015, and supported by the CLASSY analysis in Xu et al. 2022). This implies that

Table 4: Main Outflow Rates

Galaxy	$\log(\text{SFR})$ ($\text{M}_\odot \text{yr}^{-1}$)	$\log(\dot{M})$ ($\text{M}_\odot \text{yr}^{-1}$)	$\log(\eta)$	$\log(\dot{p})$ (dynes)	$\log(p_*)$ (dynes)	$\log(\eta_p)$	$\log(\dot{E})$ (erg/s)	$\log(E_*)$ (erg/s)	$\log(\eta_E)$
J0021+0052	$1.07^{+0.14}_{-0.11}$	$3.81^{+0.25}_{-1.0}$	$2.74^{+0.25}_{-1.0}$	$36.68^{+0.32}_{-1.08}$	$34.37^{+0.14}_{-0.11}$	$2.31^{+0.33}_{-1.26}$	$43.46^{+0.38}_{-1.15}$	$42.56^{+0.14}_{-0.11}$	$0.89^{+0.39}_{-1.35}$
J0036-3333	$1.01^{+0.19}_{-0.21}$	$1.07^{+0.86}_{-0.41}$	$0.06^{+0.86}_{-0.41}$	$32.78^{+1.62}_{-0.23}$	$34.31^{+0.19}_{-0.21}$	$-1.53^{+1.62}_{-0.36}$	$38.53^{+2.31}_{-0.23}$	$42.5^{+0.19}_{-0.21}$	$-3.97^{+2.31}_{-0.36}$
J0926+4427	$1.03^{+0.13}_{-0.13}$	$2.21^{+0.84}_{-0.58}$	$1.18^{+0.84}_{-0.58}$	$34.94^{+0.92}_{-0.61}$	$34.33^{+0.13}_{-0.13}$	$0.61^{+0.92}_{-0.7}$	$41.57^{+0.98}_{-0.63}$	$42.52^{+0.13}_{-0.13}$	$-0.95^{+0.98}_{-0.71}$
J0938+5428	$1.05^{+0.2}_{-0.17}$	$2.93^{+0.77}_{-0.63}$	$1.88^{+0.77}_{-0.63}$	$35.64^{+0.91}_{-0.64}$	$34.35^{+0.2}_{-0.17}$	$1.29^{+0.92}_{-0.79}$	$42.25^{+1.09}_{-0.65}$	$42.54^{+0.2}_{-0.17}$	$-0.29^{+1.09}_{-0.8}$
J1024+0524	$0.21^{+0.14}_{-0.12}$	$2.32^{+0.69}_{-0.99}$	$2.11^{+0.69}_{-0.99}$	$34.68^{+0.9}_{-0.98}$	$33.51^{+0.14}_{-0.12}$	$1.16^{+0.9}_{-1.14}$	$40.93^{+1.14}_{-0.93}$	$41.7^{+0.14}_{-0.12}$	$-0.77^{+1.14}_{-1.08}$
J1025+3622	$1.04^{+0.14}_{-0.18}$	$2.68^{+0.95}_{-0.99}$	$1.64^{+0.95}_{-0.99}$	$34.63^{+1.58}_{-0.82}$	$34.34^{+0.14}_{-0.18}$	$0.29^{+1.58}_{-1.06}$	$40.53^{+2.22}_{-0.57}$	$42.53^{+0.14}_{-0.18}$	$-2.0^{+2.22}_{-0.71}$
J1112+5503	$1.6^{+0.2}_{-0.25}$	$2.41^{+0.9}_{-0.33}$	$0.81^{+0.9}_{-0.34}$	$35.05^{+0.88}_{-0.34}$	$34.9^{+0.2}_{-0.25}$	$0.15^{+0.88}_{-0.52}$	$41.6^{+0.89}_{-0.35}$	$43.09^{+0.2}_{-0.25}$	$-1.5^{+0.89}_{-0.53}$
J1200+1343	$0.75^{+0.2}_{-0.16}$	$1.92^{+0.49}_{-0.46}$	$1.17^{+0.49}_{-0.46}$	$33.68^{+0.84}_{-0.46}$	$34.05^{+0.2}_{-0.16}$	$-0.37^{+0.84}_{-0.56}$	$39.35^{+1.34}_{-0.45}$	$42.24^{+0.2}_{-0.16}$	$-2.9^{+1.34}_{-0.55}$
J1314+3452	$-0.67^{+0.23}_{-0.55}$	$0.06^{+1.19}_{-0.57}$	$0.73^{+1.19}_{-0.57}$	$31.65^{+1.88}_{-0.52}$	$32.63^{+0.23}_{-0.55}$	$-0.98^{+1.88}_{-99.0}$	$37.15^{+2.68}_{-0.55}$	$40.82^{+0.23}_{-0.55}$	$-3.68^{+2.68}_{-99.0}$
J1359+5726	$0.42^{+0.2}_{-0.14}$	$1.68^{+1.29}_{-0.44}$	$1.26^{+1.29}_{-0.44}$	$33.37^{+1.88}_{-0.3}$	$33.72^{+0.2}_{-0.14}$	$-0.35^{+1.88}_{-0.37}$	$39.02^{+2.52}_{-0.2}$	$41.91^{+0.2}_{-0.14}$	$-2.89^{+2.52}_{-0.27}$
J1428+1653	$1.22^{+0.26}_{-0.19}$	$4.44^{+0.2}_{-0.48}$	$3.22^{+0.2}_{-0.48}$	$37.06^{+0.27}_{-0.5}$	$34.52^{+0.26}_{-0.19}$	$2.54^{+0.34}_{-0.63}$	$43.59^{+0.34}_{-0.52}$	$42.71^{+0.26}_{-0.19}$	$0.88^{+0.39}_{-0.67}$
J1429+0643	$1.42^{+0.11}_{-0.17}$	$1.85^{+0.94}_{-0.4}$	$0.43^{+0.94}_{-0.4}$	$34.4^{+1.07}_{-0.32}$	$34.72^{+0.11}_{-0.17}$	$-0.32^{+1.07}_{-0.42}$	$40.86^{+1.25}_{-0.26}$	$42.91^{+0.11}_{-0.17}$	$-2.05^{+1.25}_{-0.36}$
J1525+0757	$1.0^{+0.69}_{-0.24}$	$1.97^{+1.21}_{-0.24}$	$0.97^{+1.21}_{-0.24}$	$34.67^{+1.27}_{-0.25}$	$34.3^{+0.69}_{-0.24}$	$0.37^{+1.28}_{-0.41}$	$41.28^{+1.4}_{-0.27}$	$42.49^{+0.69}_{-0.24}$	$-1.21^{+1.41}_{-0.43}$

**Figure 3:** The predicted mass outflow rate as a function of the star-formation rate for the CLASSY galaxies.

galaxies with a larger amount of stellar production tend to eject more material into the circumgalactic medium.

6.2. Mass Outflow Factor Relations

As star formation results in the deposition of momentum and energy into the interstellar medium surrounding the star-forming regions, star-formation can be used to normalize the mass outflow rates (Chisholm et al. 2017). This normalized value is defined as $\eta = \dot{M}/\text{SFR}$, the mass loading factor.

Previously papers have noted the inverse relation between η and the mass and SFR of low-redshift galaxies (e.g. Heckman et al. 2015, Xu et al. 2022). As seen in Figure ?, we do see this correlation (though only very weakly) between these properties. There is also too much spread in the computed mass loading factor and galactic mass relationship (Figure ?) to get a good sense of how this factor changes with mass. However if we compare our results to the theoretical expectations established in the previous studies (Hayward & Hopkins

2017, Chisholm et al. 2017, and Pandya et al. 2021), our computed mass loading factor for each galaxy’s mass seen in the CLASSY galaxies is of a similar order of magnitude to the theoretical values of these previous papers (our predicted factor and the predicted loading factor using these previous works are generally off by 1-1.5 order of magnitude at maximum). Figure 5 also shows the relationship between η and SFR. Heckman et al. found an inverse correlation between these two properties, whereas we see too much scatter to extrapolate a proper trend. It should be noted that we are comparing a variable y/x with x , and thus may lead to flawed inferences.

6.3. Momentum and Energy Outflow Rates

We now have the ability to estimate the momentum and energy outflow rates for the CLASSY galaxies. The momentum outflow rate (the momentum flux carried through the outflow) is given by $\dot{p} = \dot{M}v_o$ where as the energy outflow rate (the kinetic energy flux carried through the outflow) is given by $\dot{E} = \frac{1}{2}\dot{M}v_o^2$ (Chisholm et al. 2017). We choose v_o since \dot{M} is computed at R_{SF} . The momentum and energy outflow rates are computed in this way for each ionization state of silicon, these three values are summed to get the total outflow rates of silicon and we again scale that results to hydrogen just as we did for the mass outflow rate.

This raises the question, is it reasonable to assume that a straightforward linear scaling is appropriate to convert the silicon predictions to the hydrogen prediction? Each ionization state of silicon has its own v value, which does not necessarily correlate to any of the ionization states of hydrogen. However, there is always hydrogen associated with any amount of silicon in an

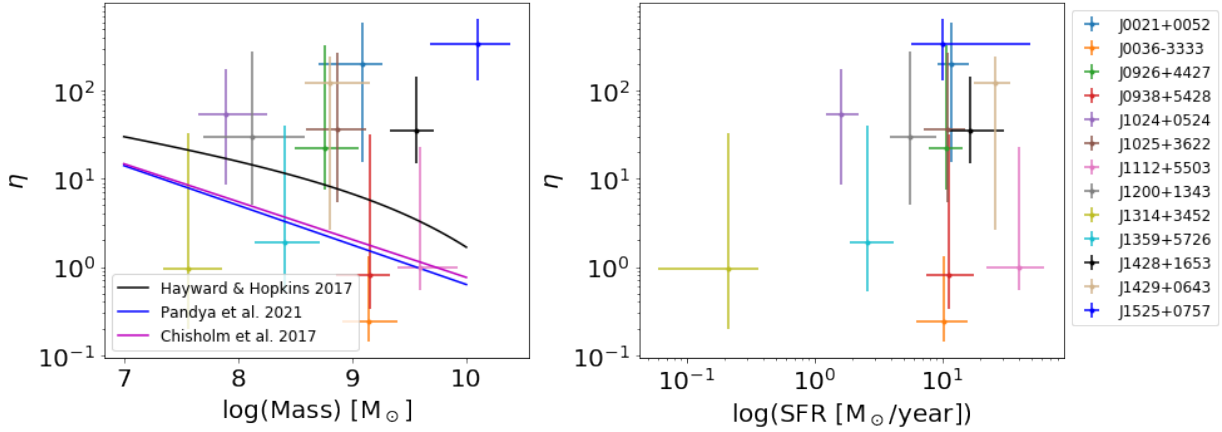


Figure 4: Left: The mass outflow factor and the total galactic mass. A few fits established in previous works are included as a reference. Right: The mass outflow factor and star-formation rate.

outflow, and therefore we believe this scaling still gives us a good estimate of these fluxes.

We compute the \dot{p} and \dot{E} values at $R_{SF} = R_{50}$, for the same reasons as mentioned in the discussion of the mass outflow rates.

In particular, it is interesting to see how these relations correlate with the momentum and kinetic energy flux deposited via starburst. Just as we normalized the mass outflow rate by the star-formation rate, the momentum and energy outflow rates can also be normalized. The momentum and energy deposition rates from supernovae are given by $\dot{p}_{SF} = 2 \times 10^{33} \left(\frac{SFR}{1 M_{\odot} \text{yr}^{-1}} \right) \text{ dynes}$ (see Murray et al. 2005) and $\dot{E}_{SF} = 3 \times 10^{41} \left(\frac{SFR}{1 M_{\odot} \text{yr}^{-1}} \right) \text{ erg/s}$ (see Leitherer et al. 1999). These relations only include direct energy and momentum deposition from supernovae, and would change with the inclusion of other factors such as stellar winds. Comparisons between \dot{p} and \dot{E} with their normalization terms can be seen in Figure 8 and Figure 9.

The momentum fluxes provided from starburst are very similar to the total estimated momentum outflow rates, indicating that momentum is transferred fairly efficiently, and that the outflows in these CLASSY galaxies are momentum driven rather than energy driven (possible exception from J808).

The normalized momentum loading factors (η_p) and energy loading factors (η_E) relationship with mass can be seen in Figure 10. While the momentum loading factor agree reasonably well with the Fire-2 simulations of Pandya et al. 2021, our estimated energy loading factor tends to be smaller than these simulations. One possible reason for this is that Pandya et al. 2021 found that the energy loading factor is much more heavily influenced by hotter gases (of order $10^5 K$ and above) than by the warm gases (of order $10^3 - 10^5 K$), of which the

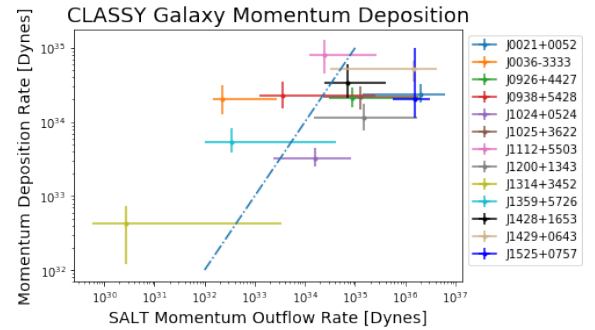


Figure 5: Estimated momentum outflow rates vs. the direct momentum deposition rate from supernovae as derived from star-formation rates. The positive correlation between the results and the fact that most galaxies lie within an order of magnitude off the one-to-one line implies an efficient transfer of momentum in these CLASSY galaxies.

SI II, III, and IV lines trace (Tumlinson et al. 2017). In contrast, Pandya et al. 2021 found that for the mass and momentum loading factors, the warm and hot gases contribute similar components. Therefore our energy loading factor may be underestimated to a large extent, as it does not consider hotter gases in its computation of the hydrogen energy outflow rate.

7. COMPARISON TO XU ET AL. (2022)

It is worth comparing these results to those presented in Xu et al. (2022), in which the mass outflow rates for the CLASSY galaxies were computed using Gaussian fitting to absorption profiles, using different assumptions including that the outflows are of constant velocity, and that $R_{SF} = 2 \times R_{50}$. Regardless of these differences, a positive correlation between the two analyses exists, as seen in Figure ?. While the magnitudes of our reported values differ, the correlation between the two is likely

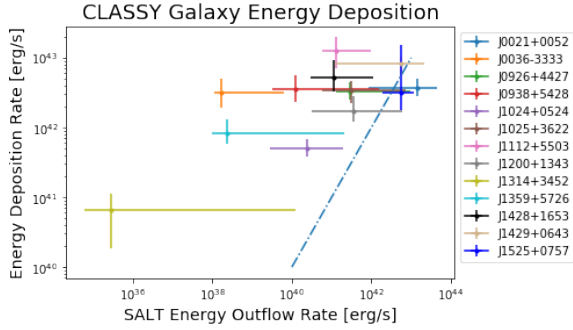


Figure 6: Estimated energy outflow rates vs. the direct energy deposition rate from supernovae as derived from star-formation rates. There does exist a positive correlation between the results, implying that as SFR increases, so does the energy outflow rate (which is logical from the mass outflow rate/star-formation rate association). However, the fact that most galaxies lie over two orders of magnitude off the one-to-one line implies there does not exist an efficient transfer of energy in most of these CLASSY galaxies. The two prominent exceptions are J0021+0052 and J1525+0757.

to capture the same trends when compared with other galactic properties.

In addition, it can be seen that these estimates generally scale proportionately with the momentum and energy outflow rate estimates of the CLASSY galaxies in Xu et al. 2022, and therefore captures the same trends (see Figure ? and Figure ?).

8. CONCLUSION

APPENDIX

A. OUTFLOW GEOMETRY PLOTS

B. SALT PARAMETER RESULTS

C. SALT FITS

D. SALT FITS

In this work, we have conducted a semi-analytical line transfer analysis upon the ultraviolet P-Cygni profiles on the local, star-forming CLASSY galaxies. From these results, we estimated these galaxies mass, momentum, and energy outflow rates.

Our primary conclusions are as follows:

- The average opening angle has a value of (INSERT AMOUNT HERE), which suggests that most outflows have large opening angles.
- The semi-analytical methods presented in this paper reveal similar trends to the Gaussian fitting techniques used in Xu et al. 2022 to analyze outflows; that said, the magnitude of these values vary.
- The mass outflow rates vary directly with star-formation rates, but there exists much scatter within these results.
- These galaxies exhibit momentum-driven behavior in their outflows rather than energy-driven.

The spread of results may indicate there is large uncertainty within these results, and while this may be true, it could also be noted as signifying the complexity and diversity amongst different galactic systems. In further work, these semi-analytical methods can be used in future for work on lines that trace hotter gas, like Carbon IV.

9. ACKNOWLEDGEMENT

We would like to acknowledge and thank the CLASSY team for their input and feedback, as well as providing the stellar continuum fits used for normalization. Mention UROP grant here.

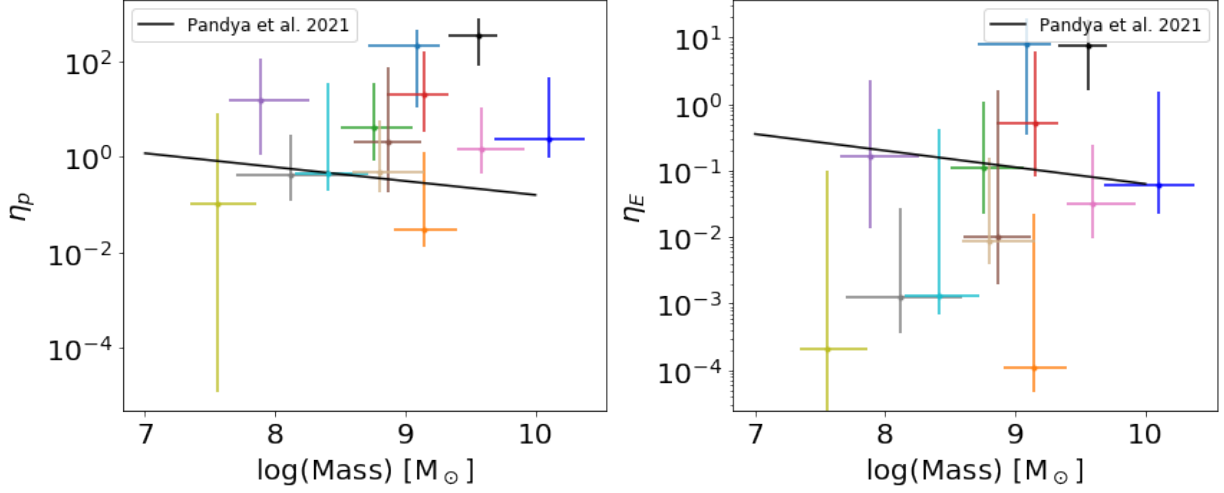


Figure 7: Left: Momentum loading factor vs. galactic mass. Right: Energy loading factor vs. galactic mass. Both plots include a black line as predicted from the Fire-2 simulations (Pandya et al. 2021). Our predicted momentum loading factor tends to agree within two orders of magnitude with the Fire-2 simulations, but the difference between the our predictions and the Fire-2 predictions for the energy loading factor is generally several orders of magnitude.

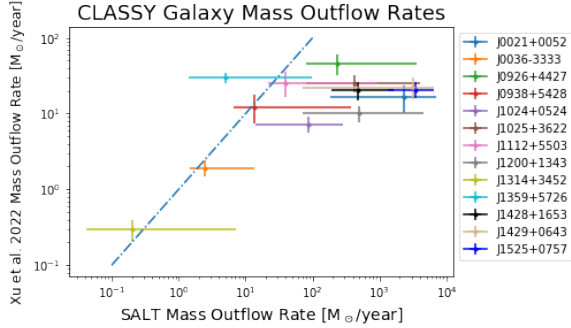


Figure 8: Comparison between the CLASSY galaxies mass outflow rates computed in Xu et al. 2022 with the outflow rates we computed given the SALT analysis. The blue line gives the one-to-one line between the two variables. While there exists a positive correlation between the two results, the magnitudes of our values tend to be larger.

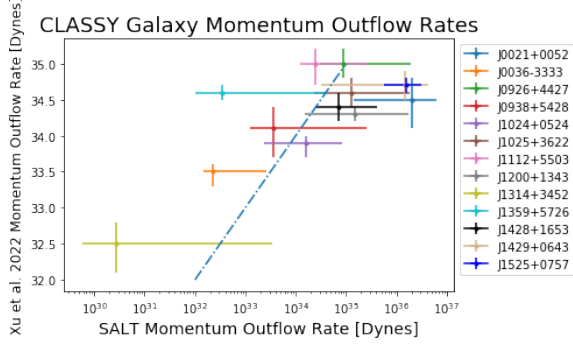


Figure 9: Our SALT predicted momentum outflow rates for the CLASSY galaxies vs. the Xu et al. 2022 predicted momentum outflow rates. While there exists a positive correlation between these two predictions, our predictions tend to be about an order of magnitude smaller.

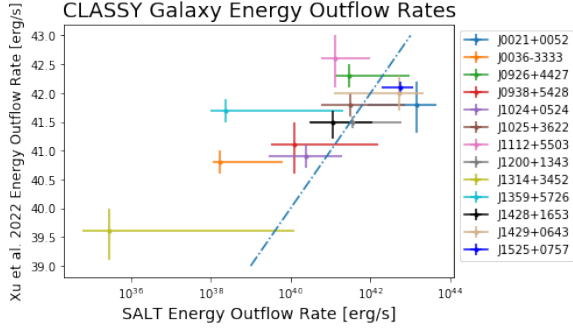


Figure 10: Our SALT predicted energy outflow rates for the CLASSY galaxies vs. the Xu et al. 2022 predicted energy outflow rates. While there exists a positive correlation between these two predictions, our predictions tend to be several orders of magnitude smaller.

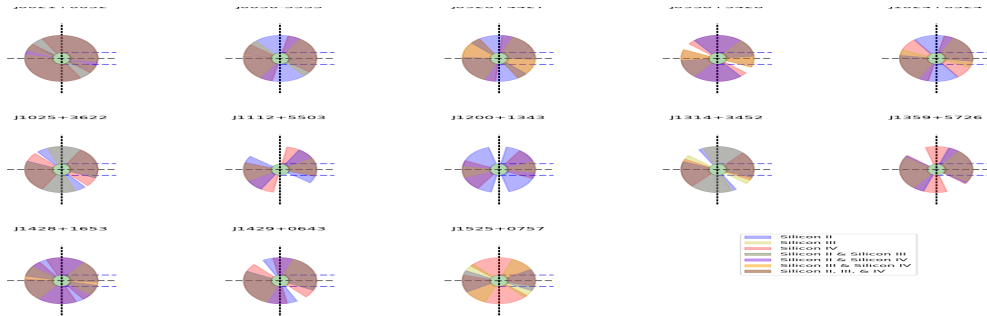


Figure 11: Composite illustrations of outflows for the 13 CLASSY galaxies that the mass outflow rates are conducted for. Large opening angles are observed in most (but not all!) ionization states of each galaxy.

Table 5: Parameter Values

Name	Ion	$\alpha(^{\circ})$	$\psi(^{\circ})$	γ	δ	$\log(\tau)$	f_c	$\log(K)$	$v_0(km/s)$	$v_w(km/s)$	$v_{ap}(km/s)$	$\log(\eta_0)$	Geometry
J0021+0052	Si II	89_{-23}^{+1}	58_{-24}^{+12}	$0.7_{-0.1}^{+0.7}$	$2.3_{-0.4}^{+1.3}$	$2.8_{-1.9}^{+0.1}$	$0.17_{-0.02}^{+0.3}$	$-0.5_{-0.8}^{+0.7}$	118_{-44}^{+15}	686_{-213}^{+174}	349_{-92}^{+721}	$-1.7_{-1.0}^{+0.1}$	
	Si III	84_{-31}^{+3}	75_{-49}^{+11}	$0.6_{-0.1}^{+0.6}$	$3.2_{-0.8}^{+0.8}$	$1.0_{-1.1}^{+0.8}$	$0.59_{-0.07}^{+0.11}$	$1.5_{-1.6}^{+0.3}$	52_{-28}^{+21}	999_{-197}^{+143}	142_{-68}^{+309}	$-3.8_{-0.7}^{+1.0}$	
	Si IV	80_{-23}^{+5}	42_{-25}^{+16}	$1.6_{-0.6}^{+0.2}$	$2.2_{-0.6}^{+0.6}$	$0.5_{-1.0}^{+0.7}$	$0.65_{-0.06}^{+0.07}$	$1.3_{-1.3}^{+0.3}$	8_{-2}^{+21}	940_{-51}^{+92}	97_{-49}^{+249}	$-5.2_{-0.5}^{+2.0}$	
J0036-3333	Si II	89_{-20}^{+1}	82_{-34}^{+2}	$0.7_{-0.1}^{+0.3}$	$2.7_{-0.4}^{+0.7}$	$1.2_{-1.0}^{+0.6}$	$0.53_{-0.07}^{+0.06}$	$-0.4_{-0.8}^{+1.0}$	17_{-3}^{+18}	623_{-105}^{+323}	51_{-8}^{+66}	$-3.6_{-0.6}^{+1.1}$	
	Si III	52_{-9}^{+18}	4_{-2}^{+20}	$1.0_{-0.2}^{+0.3}$	$2.1_{-0.2}^{+0.4}$	$-0.1_{-0.5}^{+0.9}$	$0.99_{-0.04}^{+0.0}$	$1.1_{-0.6}^{+0.5}$	9_{-4}^{+12}	568_{-36}^{+28}	48_{-18}^{+76}	$-5.0_{-0.2}^{+1.4}$	
	Si IV	57_{-11}^{+18}	20_{-9}^{+36}	$1.9_{-0.7}^{+0.1}$	$4.7_{-1.7}^{+0.1}$	$2.8_{-1.6}^{+0.1}$	$0.9_{-0.09}^{+0.03}$	$-1.0_{-0.4}^{+2.1}$	5_{-1}^{+10}	897_{-207}^{+239}	98_{-29}^{+63}	$-2.4_{-0.9}^{+0.2}$	
J0926+4427	Si II	70_{-6}^{+8}	68_{-15}^{+5}	$1.6_{-0.3}^{+0.2}$	$2.7_{-0.3}^{+1.2}$	$0.7_{-0.4}^{+0.8}$	$0.43_{-0.08}^{+0.08}$	$-1.0_{-0.5}^{+0.6}$	30_{-7}^{+18}	431_{-9}^{+44}	523_{-119}^{+320}	$-4.6_{-0.3}^{+1.4}$	
	Si III	62_{-15}^{+14}	5_{-2}^{+34}	$0.6_{-0.1}^{+0.5}$	$3.1_{-0.7}^{+0.9}$	$-1.2_{-0.3}^{+1.6}$	$0.89_{-0.12}^{+0.05}$	$-1.7_{-0.2}^{+1.4}$	140_{-71}^{+4}	761_{-160}^{+178}	416_{-130}^{+423}	$-5.8_{-0.2}^{+2.3}$	
	Si IV	71_{-20}^{+6}	13_{-7}^{+24}	$0.8_{-0.2}^{+0.4}$	$4.2_{-0.8}^{+0.3}$	$0.8_{-0.7}^{+0.5}$	$0.83_{-0.1}^{+0.07}$	$0.1_{-1.0}^{+0.7}$	85_{-28}^{+23}	952_{-214}^{+192}	364_{-95}^{+345}	$-4.0_{-0.5}^{+0.9}$	
J0938+5428	Si II	62_{-6}^{+11}	67_{-14}^{+5}	$1.5_{-0.3}^{+0.3}$	$3.9_{-1.1}^{+0.5}$	$1.7_{-0.9}^{+0.6}$	$0.76_{-0.26}^{+0.1}$	$-1.8_{-0.1}^{+0.9}$	81_{-24}^{+27}	389_{-12}^{+52}	764_{-258}^{+458}	$-3.0_{-0.6}^{+0.7}$	
	Si III	36_{-10}^{+18}	13_{-7}^{+17}	$1.8_{-0.6}^{+0.1}$	$2.9_{-0.5}^{+0.9}$	$1.0_{-1.8}^{+0.9}$	$0.38_{-0.06}^{+0.2}$	$-0.2_{-0.9}^{+1.2}$	90_{-36}^{+32}	518_{-44}^{+128}	1406_{-859}^{+518}	$-3.6_{-1.2}^{+1.2}$	
	Si IV	82_{-33}^{+4}	59_{-33}^{+12}	$1.0_{-0.5}^{+0.5}$	$4.3_{-1.1}^{+0.4}$	$-1.1_{-0.3}^{+1.0}$	$0.55_{-0.14}^{+0.18}$	$1.4_{-1.6}^{+0.3}$	145_{-72}^{+2}	804_{-255}^{+255}	657_{-315}^{+409}	$-5.6_{-0.3}^{+1.5}$	
J1024+0524	Si II	67_{-13}^{+14}	59_{-19}^{+19}	$1.4_{-0.3}^{+0.3}$	$4.8_{-1.4}^{+0.2}$	$2.5_{-2.1}^{+0.3}$	$0.73_{-0.18}^{+0.12}$	$-1.4_{-0.3}^{+0.7}$	36_{-10}^{+29}	203_{-62}^{+17}	186_{-21}^{+154}	$-2.3_{-1.0}^{+0.4}$	
	Si III	42_{-8}^{+17}	19_{-10}^{+15}	$1.5_{-0.5}^{+0.2}$	$3.6_{-0.7}^{+0.5}$	$0.3_{-0.8}^{+1.4}$	$0.87_{-0.09}^{+0.05}$	$1.2_{-1.2}^{+0.5}$	11_{-4}^{+21}	332_{-63}^{+59}	66_{-28}^{+119}	$-5.0_{-0.5}^{+2.3}$	
	Si IV	65_{-17}^{+15}	12_{-6}^{+26}	$0.7_{-0.1}^{+0.7}$	$2.1_{-0.3}^{+1.4}$	$-0.9_{-0.4}^{+0.9}$	$0.68_{-0.07}^{+0.14}$	$1.1_{-1.0}^{+0.5}$	30_{-12}^{+18}	869_{-318}^{+172}	67_{-23}^{+143}	$-5.7_{-0.2}^{+1.3}$	

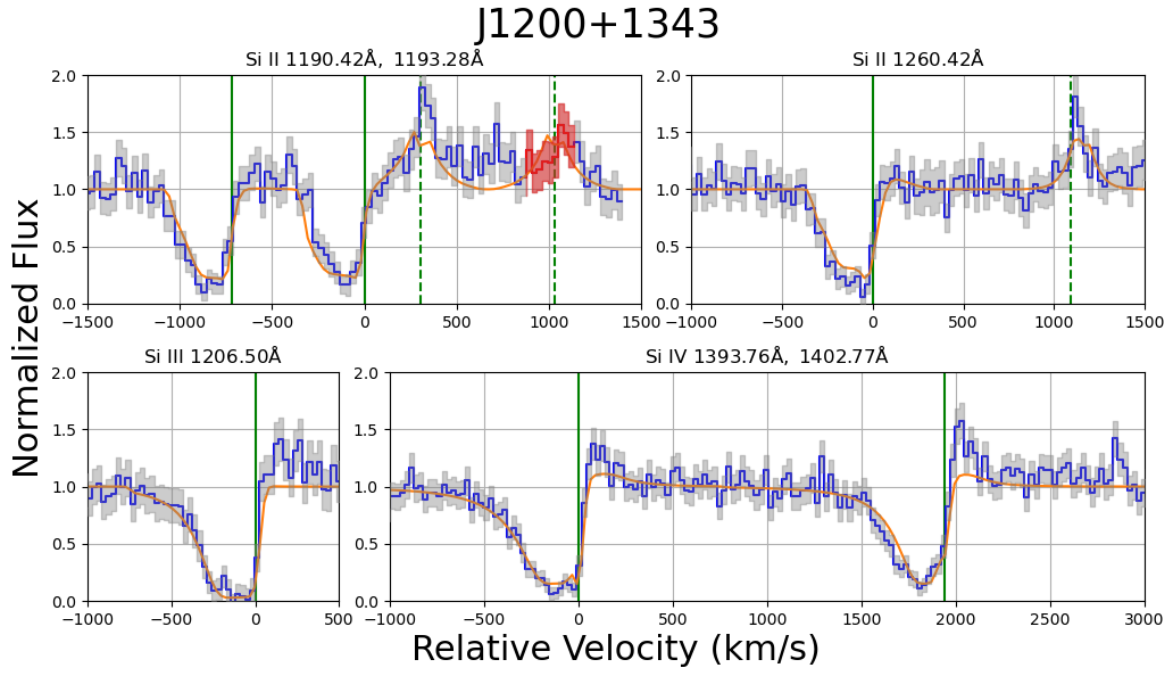


Figure 12: SALT fits for J.

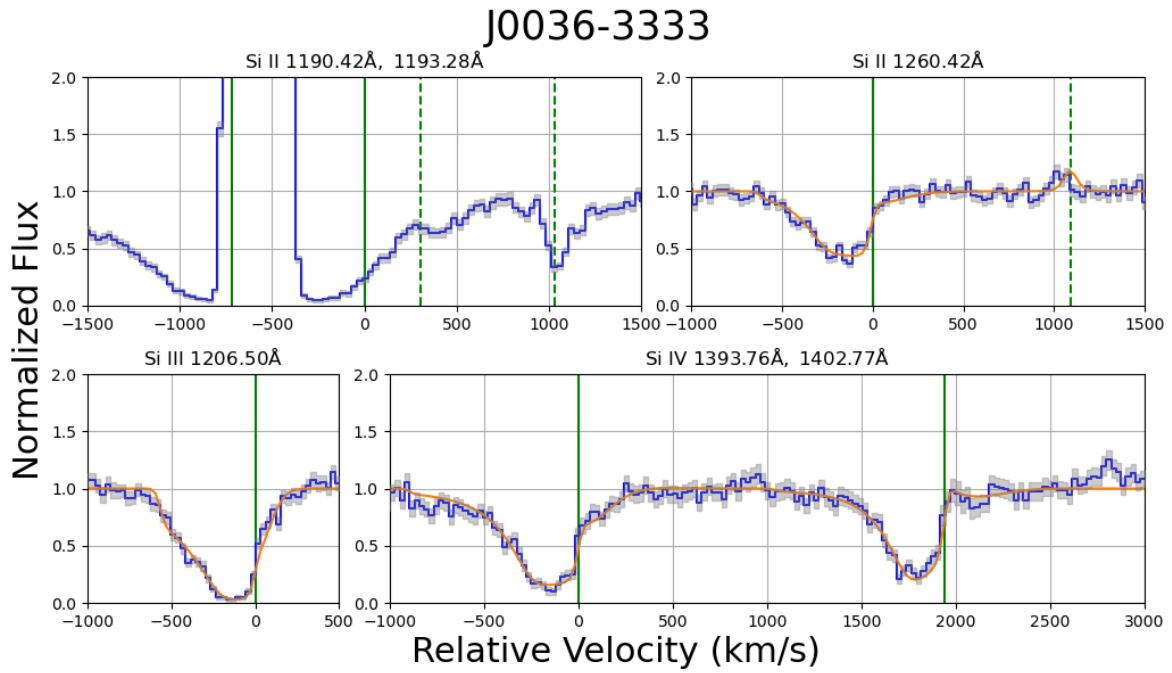


Figure 13: SALT fits for J.

REFERENCES

- Berg, D. A., James, B. L., King, T., et al. 2022, *ApJS*, 261, 31. doi:10.3847/1538-4365/ac6c03
- Burchett, J. N., Rubin, K. H. R., Prochaska, J. X., et al. 2021, *ApJ*, 909, 151. doi:10.3847/1538-4357/abd4e0
- Calzetti, D. 1997, The ultraviolet universe at low and High redshift, 408, 403. doi:10.1063/1.53764
- Carr, C., Scarlata, C., Panagia, N., et al. 2018, *ApJ*, 860, 143. doi:10.3847/1538-4357/aac48e
- Carr, C., Scarlata, C., Henry, A., et al. 2021, *ApJ*, 906, 104. doi:10.3847/1538-4357/abc7c3
- Carr, C. & Scarlata, C. 2022, arXiv:2209.14485
- Chisholm, J., Tremonti, C. A., Leitherer, C., et al. 2017, *MNRAS*, 469, 4831. doi:10.1093/mnras/stx1164
- Chisholm, J., Bordoloi, R., Rigby, J. R., et al. 2018, *MNRAS*, 474, 1688. doi:10.1093/mnras/stx2848
- Foreman-Mackey, D., Hogg, D. W., Lang, D., et al. 2013, *PASP*, 125, 306. doi:10.1086/670067
- Hayward, C. C. & Hopkins, P. F. 2017, *MNRAS*, 465, 1682. doi:10.1093/mnras/stw2888
- Heckman, T. M., Alexandroff, R. M., Borthakur, S., et al. 2015, *ApJ*, 809, 147. doi:10.1088/0004-637X/809/2/147
- Hopkins, P. F., Kereš, D., Oñorbe, J., et al. 2014, *MNRAS*, 445, 581. doi:10.1093/mnras/stu1738
- Ivezić, Ž., Connolly, A. J., VanderPlas, J. T., et al. 2014, *Statistics, Data Mining, and Machine Learning in Astronomy*, by Z. Ivencić et al. Princeton, NJ: Princeton University Press, 2014
- Leitherer, C., Schaerer, D., Goldader, J. D., et al. 1999, *ApJS*, 123, 3. doi:10.1086/313233
- Martin, C. L. 2005, *ApJ*, 621, 227. doi:10.1086/427277
- McKinney, J. H., Jaskot, A. E., Oey, M. S., et al. 2019, *ApJ*, 874, 52. doi:10.3847/1538-4357/ab08eb
- Murray, N., Quataert, E., & Thompson, T. A. 2005, *ApJ*, 618, 569. doi:10.1086/426067
- Pandya, V., Fielding, D. B., Anglés-Alcázar, D., et al. 2021, *MNRAS*, 508, 2979. doi:10.1093/mnras/stab2714
- Rubin, K. H. R. 2017, *Gas Accretion onto Galaxies*, 430, 95. doi:10.1007/978-3-319-52512-9_5
- Scarlata, C. & Panagia, N. 2015, *ApJ*, 801, 43. doi:10.1088/0004-637X/801/1/43
- Shapley, A. E., Steidel, C. C., Pettini, M., et al. 2003, *ApJ*, 588, 65. doi:10.1086/373922
- Tumlinson, J., Peebles, M. S., & Werk, J. K. 2017, *ARA&A*, 55, 389. doi:10.1146/annurev-astro-091916-055240
- Xu, X., Heckman, T., Henry, A., et al. 2022, arXiv:2204.09181